

Biases of estimated signals in x-ray analyzer-based imaging

Jianlin Xia(夏健霖), Wen Xu(徐文), Ruicheng Zhou(周瑞成), Xiaomin Shi(石晓敏), Kun Ren(任坤), Heng Chen(陈恒), Zhili Wang(王志立)

Citation: Chin. Phys. B . 2020, 29(6): 068703 . **doi:** 10.1088/1674-1056/ab8887
Journal homepage: http://cpb.iphy.ac.cn; http://iopscience.iop.org/cpb

What follows is a list of articles you may be interested in

Theory and method of dual-energy x-ray grating phase-contrast imaging

Feng Rong(荣锋), Yan Gao(高艳), Cui-Juan Guo(郭翠娟), Wei Xu(徐微), Wei Xu(徐伟)

Chin. Phys. B . 2019, 28(10): 108702 . **doi:** 10.1088/1674-1056/ab3f1d

Shifting curves based on the detector integration effect for x-ray phase contrast imaging

Jun Yang(杨君), Jin-Chuan Guo(郭金川), Yao-Hu Lei(雷耀虎), Ming-Hao Yi(易明皓), Li Chen(陈力)

Chin. Phys. B . 2017, 26(2): 028701 . **doi:** 10.1088/1674-1056/26/2/028701

Elemental x-ray imaging using Zernike phase contrast

Qi-Gang Shao(邵其刚), Jian Chen(陈健), Faiz Wali, Yuan Bao(鲍园), Zhi-Li Wang(王志立), Pei-Ping Zhu(朱佩平), Yang-Chao Tian(田扬超), Kun Gao(高昆)

Chin. Phys. B . 2016, 25(10): 108702 . **doi:** 10.1088/1674-1056/25/10/108702

Simple phase extraction in x-ray differential phase contrast imaging

Xin Liu(刘鑫), Jin-Chuan Guo(郭金川), Yao-Hu Lei(雷耀虎), Ji Li(李冀), Han-Ben Niu(牛憨笨)

Chin. Phys. B . 2016, 25(2): 028704 . **doi:** 10.1088/1674-1056/25/2/028704

Investigation of noise properties in grating-based x-ray phase tomography with reverse projection method

Bao Yuan, Wang Yan, Gao Kun, Wang Zhi-Li, Zhu Pei-Ping, Wu Zi-Yu

Chin. Phys. B . 2015, 24(10): 108702 . **doi:** 10.1088/1674-1056/24/10/108702

Biases of estimated signals in x-ray analyzer-based imaging*

Jianlin Xia(夏健霖), Wen Xu(徐文), Ruicheng Zhou(周瑞成), Xiaomin Shi(石晓敏), Kun Ren(任坤), Heng Chen(陈恒), and Zhili Wang(王志立)†

School of Electronic Science & Applied Physics, Hefei University of Technology, Hefei 230009, *China*

(Received 15 December 2019; revised manuscript received 2 April 2020; accepted manuscript online 12 April 2020)

Recently, a novel three-image algorithm has been proposed to retrieve the sample's absorption, refraction, and scattering properties in x-ray analyzer-based imaging. The feasibility of the three-image algorithm was validated by synchrotron radiation experiments. However, it is unclear yet whether the estimated refraction and scattering signals are biased or not and how the analyzer angular position affects the biases in the estimated signals. For this purpose, the biases of the extracted refraction and scattering signals are theoretically derived for the three-image algorithm. The theoretical models are further confirmed by numerical experiments. The results show that both the estimated refraction and scattering signals are biased, and the biases are strongly dependent on the analyzer angular position. Besides, the biases also show dependence on the sample's refraction and scattering properties locally. Those results can be used as general guidelines to optimize experimental parameters for bias reduction and accurate imaging of different features within the sample.

Keywords: x-ray imaging, analyzer-based imaging, three-image algorithm

PACS: 87.59.–e, 43.60.Cg, 42.30.Rx, 41.50.+h **DOI:** 10.1088/1674-1056/ab8887

1. Introduction

Over the past two decades, x-ray analyzer-based imaging (ABI) has attracted great interest in the scientific community.[1] Compared to conventional absorption-based x-ray imaging, it can generate additional contrast from the sample's refraction and ultra-small-angle x-ray scattering (USAXS) properties.[2–7] Recently, a novel three-image algorithm has been proposed to retrieve the sample's absorption, refraction, and scattering signals in x-ray ABI.[8] In comparison to multiple-image radiography,[9,10] the three-image algorithm has the advantage of decreased acquisition time and possible dose reduction.

However, one question we cannot ignore is that whether the signals retrieved by the three-image algorithm are accurate enough. Quite recently, the biases of the estimated signals have been studied in grating-based differential phase contrast imaging.[11] However, the biases of the estimated signals in x-ray analyzer-based imaging are not clear yet. And that is the purpose of the present work.

For further analysis, we introduce $E(\Delta\hat{\theta})$ and $E(\hat{\sigma}_s^2)$ as the mean of estimated refraction and scattering signals, respectively. Note that $E(\Delta\hat{\theta})$ and $E(\hat{\sigma}_s^2)$ can be calculated from repeated experiments. And then, the biases of estimated signals can be expressed as

$$\begin{cases} b_{\Delta\hat{\theta}} = E\left(\Delta\hat{\theta}\right) - \Delta\bar{\theta}, \\ b_{\hat{\sigma}_s^2} = E\left(\hat{\sigma}_s^2\right) - \bar{\sigma}_s^2, \end{cases} \tag{1}$$

where $\Delta\bar{\theta}$ and $\bar{\sigma}_s^2$ represent the retrieved sample's refraction and scattering signals, respectively, from $\bar{I}_k$ ($k = 1, 2, 3$) by the three-image algorithm,[8] with $\bar{I}_k$ being the expected x-ray intensity measured at a given analyzer angular position. Note that if $b_{\Delta\hat{\theta}}$ and $b_{\hat{\sigma}_s^2}$ have a zero value, the novel three-image algorithm is defined as an unbiased estimator. Otherwise, this algorithm is a biased estimator.

To the best of our knowledge, the potential bias of the estimated refraction and scattering signals in x-ray ABI has not yet been fully studied in the literature. The aim of the present work is to perform both theoretical and experimental studies on this important topic. The dependence of signal biases on the analyzer angular position and the sample's properties is investigated. Those obtained results can be useful to guide experimental design and optimization.

2. Methods

2.1. Brief review of the three-images algorithm

Based on fitting the intrinsic rocking curve (RC) with a Gaussian function,[8] we can yield the following expression for the measured intensity in x-ray analyzer-based imaging:

$$I_k(x,y) = I_0\sigma_\theta \frac{I_R(x,y)}{\sigma(x,y)} \exp\left\{-\frac{[\theta_k - \Delta\theta(x,y)]^2}{2\sigma^2(x,y)}\right\}, \quad (k = 1,2,3), \tag{2}$$

where I_0 defines the incident photon number per pixel, σ_θ is the standard deviation of the intrinsic rocking curve, I_R represents the sample's apparent absorption, $\Delta\theta$ is the sample's refraction, and σ_s^2 represents the sample's scattering and

*Project supported by the National Natural Science Foundation of China (Grant Nos. U1532113, and 11475170) and the Fundamental Research Funds for the Central Universities, China (Grant No. PA2020GDKC0024).

†Corresponding author. E-mail: dywangzl@hfut.edu.cn

© 2020 Chinese Physical Society and IOP Publishing Ltd

$\sigma^2 = \sigma_\theta^2 + \sigma_s^2$. With three different intensities measured at three distinct angular positions of the analyzer crystal, one can retrieve the sample's absorption, refraction, and scattering signals by

$$\begin{cases} \hat{I}_R(x,y) = \dfrac{I_2|\theta_1|}{I_0\sigma_\theta}\dfrac{1}{\sqrt{C_1+C_2}}\exp\left[\dfrac{1}{8}\dfrac{(C_1-C_2)^2}{C_1+C_2}\right], \\ \Delta\hat{\theta}(x,y) = \dfrac{\theta_1}{2}\dfrac{C_2-C_1}{C_1+C_2}, \\ \hat{\sigma}_s^2(x,y) = \dfrac{\theta_1^2}{C_1+C_2} - \sigma_\theta^2, \end{cases} \tag{3}$$

where $C_1 = \ln(I_2/I_1)$ and $C_2 = \ln(I_2/I_3)$. Detailed derivations of Eq. (2) can be found in the literature.[8]

2.2. Biases of estimated signals by the three-images algorithm

If $\hat{\theta}$ is the estimator extracted from $\boldsymbol{x}$, which is a series of measured data, we can use the second-order Taylor series expansion to approximate $\hat{\theta}(\boldsymbol{x})$ around $\bar{\boldsymbol{x}}$:[11]

$$\begin{aligned} \hat{\theta} \approx\ & \hat{\theta}(\bar{\boldsymbol{x}}) + \sum_i \left.\frac{\partial\hat{\theta}}{\partial x_i}\right|_{\bar{\boldsymbol{x}}}(x_i-\bar{x}_i) + \frac{1}{2}\sum_i \left.\frac{\partial^2\hat{\theta}}{\partial x_i\partial x_j}\right|_{\bar{\boldsymbol{x}}} \\ & \times (x_i-\bar{x}_i)(x_j-\bar{x}_j), \end{aligned} \tag{4}$$

where x_i is the i-th element in the data vector $\boldsymbol{x}$. Under this approximation the mean of estimated signal, $E\left[\hat{\theta}(\boldsymbol{x})\right]$ can be written as:

$$\begin{aligned} E\left[\hat{\theta}(\boldsymbol{x})\right] \approx\ & E\left\{\hat{\theta}(\bar{\boldsymbol{x}}) + \sum_i \left.\frac{\partial\hat{\theta}}{\partial x_i}\right|_{\bar{\boldsymbol{x}}} E(x_i-\bar{x}_i)\right. \\ & \left. + \frac{1}{2}\sum_i \left.\frac{\partial^2\hat{\theta}}{\partial x_i\partial x_j}\right|_{\bar{\boldsymbol{x}}} E\left[(x_i-\bar{x}_i)(x_j-\bar{x}_j)\right]\right\}. \end{aligned} \tag{5}$$

In the case of x-ray analyzer-based imaging, $\hat{\theta}(\bar{\boldsymbol{x}})$ corresponds to the signals extracted from the intensity measurements by the three-image algorithm, and $\boldsymbol{x}$ contains the experimentally measured intensities. Note that the elements of $\boldsymbol{x}$ are statistically uncorrelated. Then the following results can be readily derived

$$\begin{cases} \hat{\theta}(\bar{\boldsymbol{x}}) = \theta, \\ \langle x_i - \bar{x}_i\rangle = 0, \\ \left\langle (x_i-\bar{x}_i)(x_j-\bar{x}_j)\right\rangle = \mathrm{cov}(x_i,x_j) = \sigma_{x_i}^2\delta_{ij}, \end{cases} \tag{6}$$

where $\sigma_{x_i}^2$ represent the variance of x_i, δ_{ij} is the Kronecker delta, and θ means the truth value. From Eq. (5) and Eq. (6) one can derive the expression for the estimated signal bias:

$$b(\hat{\theta}) = E(\hat{\theta}-\theta) \approx E(\hat{\theta}-\bar{\theta}) \approx \frac{1}{2}\sum_i \left.\frac{\partial^2\hat{\theta}}{\partial x_i^2}\right|_{\bar{\boldsymbol{x}}}\sigma_{x_i}^2. \tag{7}$$

Obviously, the bias of the estimated signal is affected by the variance of x_i and the second-order derivative of $\hat{\theta}$ based on the expectation $\bar{\boldsymbol{x}}$. Using Eq. (7) and Eq. (3), we can calculate the biases of the estimated refraction and scattering signals as follows:

$$\begin{cases} b_{\Delta\hat{\theta}} = f(\theta_1) + 4f(0) + f(-\theta_1), \\ b_{\hat{\sigma}_s^2} = g(\theta_1) + 4g(0) + g(-\theta_1), \end{cases} \tag{8}$$

where

$$\begin{cases} f(x) = \dfrac{\left(2\Delta\bar{\theta}+x\right)g(x)}{\bar{\sigma}^2}, \\ g(x) = \dfrac{\bar{\sigma}^5\left(4\bar{\sigma}^2-3x^2+\theta_1^2\right)}{8I_0\sigma_\theta\bar{I}_R\theta_1^4}\exp\left[\dfrac{\left(x-\Delta\bar{\theta}\right)^2}{2\bar{\sigma}^2}\right], \end{cases} \tag{9}$$

where $\bar{\sigma}^2 = \bar{\sigma}_s^2 + \sigma_\theta^2$. In Eq. (9), $\Delta\bar{\theta}$, $\bar{\sigma}_s^2$, and $\bar{I}_R$ represent signals extracted from mean intensities $\bar{I}_k$ ($k = 1, 2, 3$), which were obtained by averaging a mass of intensity measurements at the same analyzer angular position. Detailed derivation of Eq. (8) can be found in Appendix A. As shown in Eq. (8), the biases of estimated refraction and scattering signals can be regarded as the sum of certain functions at three analyzer angular positions. Both the refraction bias $\left(b_{\Delta\hat{\theta}}\right)$ and the scattering bias $\left(b_{\hat{\sigma}_s^2}\right)$ are inversely proportional to the sample's absorption and the incident photon number per pixel. They are also dependent on the $\Delta\bar{\theta}$ and $\bar{\sigma}_s^2$ locally and the analyzer angular position θ_1. In the following, numerical experiments are performed to validate the theoretical models given in Eq. (8), and to provide some quantitative insights into how the analyzer angular position affects the biases of retrieved refraction and scattering signals.

3. Numerical results and discussions

3.1. Numerical phantom and imaging parameters

A simulation phantom which consists of a PMMA rod lying in front of scatter foils was constructed following Refs. [12–16]. The real part of refraction index of the PMMA rod, δ, has a value of $\delta = 9.21\times10^{-7}$ at 17 keV.[17] In addition to refraction, the PMMA rod also features absorption quantified by the attenuation coefficient $\mu = 0.94\ \mathrm{cm}^{-1}$ at 17 keV.[17] The incident photon number was assumed to 2.5×10^4 per pixel.[17,18]

The PMMA rod, which provides absorption and refraction signals, has a diameter of 6 mm and a length of 12.5 mm, with a series of scatter foils superimposed at the back of PMMA rod.[19] These foils, 2.5-mm width and 10-mm high, have been assumed as homogenous, non-absorbing and non-refraction papers. Those papers with the textile structure, are characterized by different scattering distributions with standard deviation σ_s ranging from 0 μrad to 21.41 μrad (namely 0 μrad, 6.42 μrad, 12.85 μrad, 17.13 μrad, and 21.41 μrad), which corresponds to a full width at half maximum (FWHM)

from 0 μrad to 50 μrad (thus 0-, 15-, 20-, 30-, and 50-μrad FWHM).[20] This range was chosen to study the influence of this parameter in the applicability of the algorithm covering scattering distribution widths much smaller, comparable and significantly larger than σ_θ of Si (111) analyzer RC ($\sim$ 8.6 μrad) at 17 keV.[17] The required three intensity measurements are simulated using Eq. (2), and the phantom's absorption, refraction, and scattering signals are retrieved by the three-image algorithm, *i.e.*, Eq. (3).

3.2. Biases of estimated signals

Once we reconstruct the image of $E(\Delta\hat{\theta})$ and $E(\hat{\sigma}_s^2)$, the biases of refraction and scattering signals can be readily derived, and the results are shown in Fig. 1. Then we can compare them to the theoretical predictions drawn from Eq. (8), as depicted in Fig. 2. As demonstrated in Figs. 1 and 2, the numerical results are always in good agreement with our theoretical predictions. Those results confirm the validity of the theoretical models ofestimated signals biases.

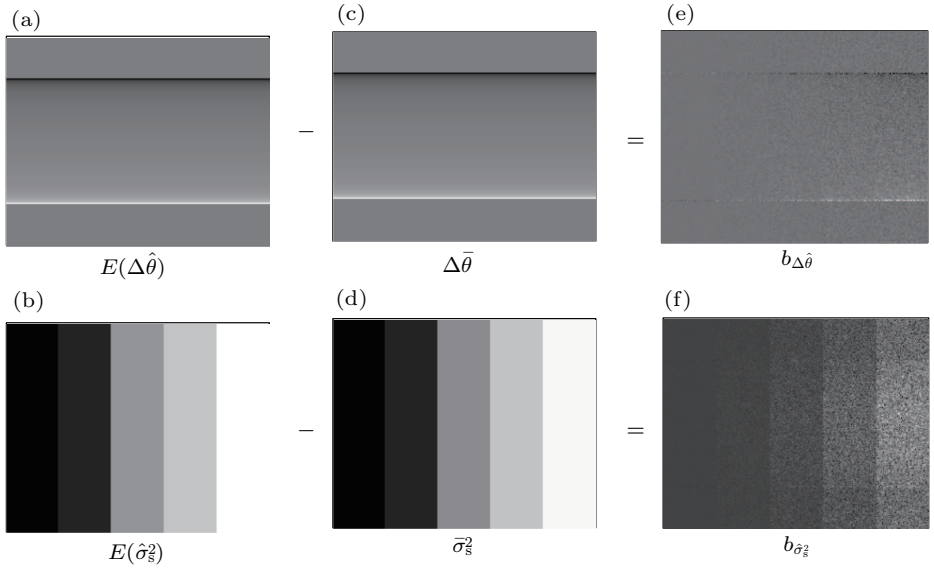


Fig. 1. Simulated phantom images. Panels (a) and (b) are average images of $\Delta\hat{\theta}$ and $\hat{\sigma}_s^2$, panels (c) and (d) represent the images of $\Delta\bar{\theta}$ and $\bar{\sigma}_s^2$, panels (e) and (f) are images of $b_{\Delta\hat{\theta}}$ and $b_{\hat{\sigma}_s^2}$.

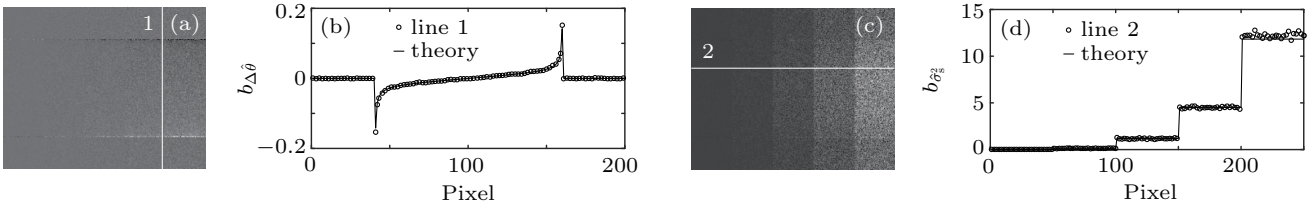


Fig. 2. Line 1 in panel (a) is vertical profiles of $b_{\Delta\hat{\theta}}$ from Fig. 1(e) with $\bar{\sigma}_s$ being 17.13 μrad, line 2 in panel (c) means horizontal profiles of $b_{\hat{\sigma}_s^2}$ in PMMA where $\Delta\bar{\theta}$ is -6.18 μrad. They are all drawn as discrete points in panels (b) and (d), and solid lines represent the theoretical biases derived from Eq. (8).

To further study the bias of estimated signals, the bias is plotted as a function of the refraction signal for different scattering signals. As shown in Fig. 3, the overall amplitude of the biases in estimated refraction and scattering signals, $\left|b_{\Delta\hat{\theta}}\right|$ and $\left|b_{\hat{\sigma}_s^2}\right|$, become larger when $\left|\Delta\bar{\theta}\right|$ increases. This indicates that the reconstructed parametric images become more accurate with a decrease in the amplitude of the refraction angle. Figure 3 also shows that for a fixed refraction signal, the amplitude of the biases increases with the scattering signal. It is noteworthy that those results are quite similar to those obtained in grating-based differential phase contrast imaging by using the phase stepping (PS) method.[21] The similarity of the two phase-contrast imaging methods is not surprising as they are both sensitive to the same physical quantities: the refraction angle and the refractive scattering angle.[4,22]

Based upon the above results, if one hopes to keep the signal biases negligible, then a minimal amount of exposure is required. Equations (8) and (9) can be used as a guideline to set such a minimal exposure level. Consider an example, where the relative bias of the scattering signals is required to be smaller than 1% for the range of $\Delta\bar{\theta} \in [-12\ \mu\text{rad}, 12\ \mu\text{rad}]$, $\bar{\sigma}_s \in [0, 15\ \mu\text{rad}]$, and $\bar{I}_R \in [0.4, 0.9]$.[11] As shown in Fig. 3, the maximum bias of the scattering signals occurred with $\Delta\bar{\theta} = \pm 12$ μrad, $\bar{\sigma}_s = 15$ μrad, and $\bar{I}_R = 0.4$. By using Eqs. (8) and (9), the number of incident photons per pixel must be larger than the following lower limit, $(I_0)_{\min}$,

$$(I_0)_{\min} \approx 5 \times 10^4, \tag{10}$$

as shown in Fig. 4.

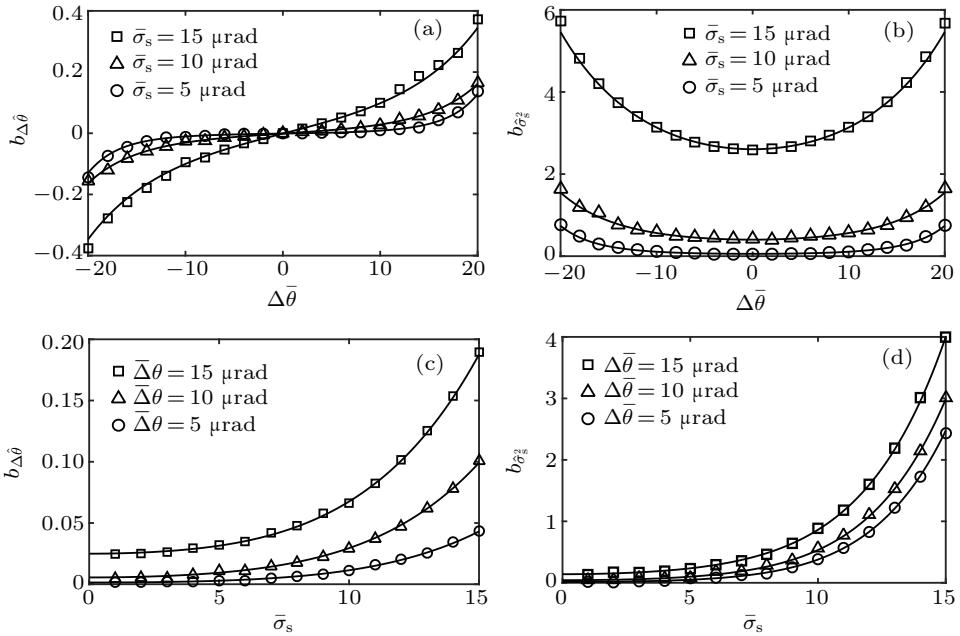


Fig. 3. (a) Bias of refraction and (b) bias of scattering *versus* refraction angle. The discrete points represent the experimental results and the solid lines are the theoretical predictions from Eq. (8). Circles, triangles, and squares correspond, respectively, to three different scattering signals: 5 μrad, 10 μrad, and 15 μrad. (c) Bias of refraction and (d) bias of scattering *versus* scattering signal. Circles, triangles, and squares correspond, respectively, to three different refraction angles: 5 μrad, 10 μrad, and 15 μrad.

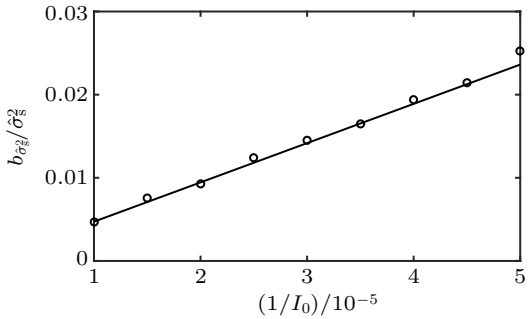


Fig. 4. The relative bias of scattering signals ($b_{\hat{\sigma}_s^2}/\hat{\sigma}_s^2$) *versus* the reciprocal of I_0. Clearly, the bias of scattering is less than 1% when the number of incident photons is over 5×10^4.

3.3. Effect of the analyzer angular position

Furthermore, it is of much practical significance to study the dependence of signal biases on the analyzer angular position θ_1. This can serve as a guide to optimize the data acquisition scheme. Actually, the value of σ_θ depends on the analyzer crystal and the x-ray energy. Therefore, we consider the two ratios $b_{\Delta\hat{\theta}}/\sigma_\theta$ and $b_{\hat{\sigma}_s^2}/\sigma_\theta^2$, which can be obtained from Eq. (8). Note that equation (8) is an even function of θ_1. Therefore, the following figures are plotted only in a negative range of θ_1/σ_θ with $\Delta\bar{\theta}/\sigma_\theta = 0.1$, 1.0, and $\bar{\sigma}_s/\sigma_\theta = 0.1$, 1.0, respectively.

As shown in Fig. 5, the biases of both refraction and scattering signals can reach their minimum at different analyzer angular positions. And those positions are dependent on the sample's refraction and scattering properties. Besides, figures 5(a) and 5(b) are similar to some extent, which indicates that if the refraction signal is optimized at a certain angular position, the scattering signal still has a high accuracy at the same position, however it is not optimal. This means that it is possible to obtain highly accurate refraction and scattering signals simultaneously at a certain analyzer position. Figure 5(b) also shows that for the retrieved scattering signals, compared to the case of refraction, the optimal analyzer angular position where the signal bias achieves its minimum depends more closely on the object's scattering properties locally.

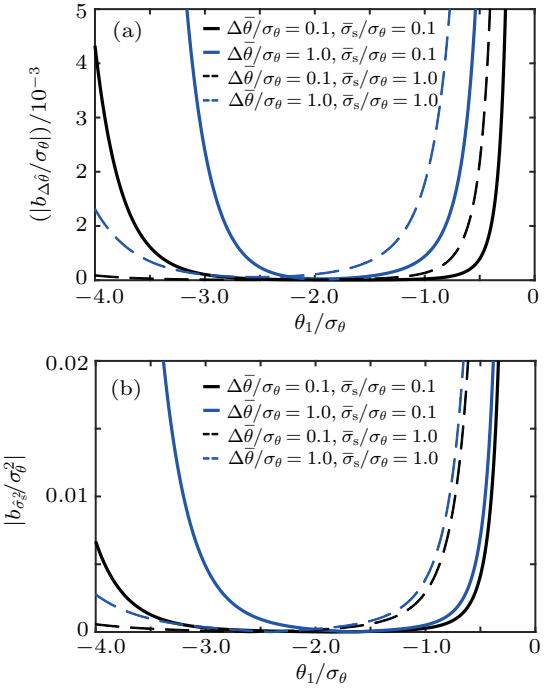


Fig. 5. Bias of refraction (a) and scattering (b) *versus* θ_1/σ_θ for different refraction and scattering signals.

In order to improve the quality of the extracted signals, two approaches can thus be considered. The first is to increase

the incident photon number, which can be achieved by increasing x-ray tube current or exposure time. While the radiation dose is always an important factor in clinical imaging applications, a trade-off has to be considered between the incident photon number and image quality. Another option is to choose an optimal analyzer position for the parameter to be estimated in a selected region of interest. We have presented analytical formals to determine the optimal analyzer angular position to minimize the estimation biases in x-ray analyzer-based imaging, although it still remains to be verified by experimental results. And this will be our future work.

4. Conclusion

In conclusion, the potential biases for the estimated refraction and scattering signals in x-ray analyzer-based imaging have been investigated. Analytical expressions were derived to quantify the level of biases and the dependence of biases on experimental parameters. The theoretical results were validated via numerical experiments. The results showed that both the estimated refraction and scattering signals were biased, and the level of biases was dependent on the incident intensity, the sample's properties, and especially the analyzer angular position. Those results can be used as guidelines to optimize acquisition parameters for bias reduction in x-ray analyzer-based imaging.

Appendix A: Detailed derivation of Eq. (8)

From Eq. (7), we can obtain the expression of refraction bias:

$$b_{\Delta\hat{\theta}} = \frac{1}{2}\left(\frac{\partial^2 \Delta\hat{\theta}}{\partial \left(I_1\right)^2}\Big|_{\bar{I}_1} \sigma_{I_1}^2 + \frac{\partial^2 \Delta\hat{\theta}}{\partial \left(I_2\right)^2}\Big|_{\bar{I}_2} \sigma_{I_2}^2 + \frac{\partial^2 \Delta\hat{\theta}}{\partial \left(I_3\right)^2}\Big|_{\bar{I}_3} \sigma_{I_3}^2 \right). \tag{A1}$$

For quantum-limited photon-counting x-ray imaging systems, the recorded number follows the Poisson distribution, which means that the variance of I_k is equal to its mean value, namely,

$$\sigma_{I_k}^2 = \bar{I}_k = I_0 \sigma_\theta \frac{I_{\mathrm{R}}(x,y)}{\sigma(x,y)} \exp\left\{ -\frac{\left[\theta_k - \Delta\theta(x,y)\right]^2}{2\sigma^2(x,y)} \right\}, \quad (k=1,2,3). \tag{A2}$$

The refraction estimator bias is then calculated as follows:

$$\begin{aligned}
b_{\Delta\hat{\theta}} &= \frac{1}{2}\left[\frac{\theta_1 C_2 (2 - C_2 - C_1)}{(C_2+C_1)^3 \bar{I}_1} + \frac{\theta_1 (C_2 - C_1)(C_2 + C_1 + 4)}{(C_2+C_1)^3 \bar{I}_2} + \frac{\theta_1 C_1 (C_2 + C_1 - 2)}{(C_2+C_1)^3 \bar{I}_3} \right] \\
&= \frac{1}{2}\left\{ \frac{\bar{\sigma}^3 (\theta_1 + 2\Delta\theta)\left(2\bar{\sigma}^2 - \theta_1^2\right)}{2I_0\sigma_\theta I_{\mathrm{R}} \theta_1^4} \exp\left[\frac{(\theta_1 - \Delta\theta)^2}{2\bar{\sigma}^2} \right] + \frac{2\bar{\sigma}^3 \Delta\theta \left(4\bar{\sigma}^2 + \theta_1^2\right)}{I_0\sigma_\theta I_{\mathrm{R}} \theta_1^4} \exp\left[\frac{(\Delta\theta)^2}{2\bar{\sigma}^2} \right] \right. \\
&\quad \left. + \frac{\bar{\sigma}^3 (\theta_1 - 2\Delta\theta)\left(\theta_1^2 - 2\bar{\sigma}^2\right)}{2I_0\sigma_\theta I_{\mathrm{R}} \theta_1^4} \exp\left[\frac{(\theta_1 + \Delta\theta)^2}{2\bar{\sigma}^2} \right] \right\} \\
&= \frac{\bar{\sigma}^3}{4I_0\sigma_\theta I_{\mathrm{R}} \theta_1^4} \left\{ (\theta_1 + 2\Delta\theta)\left(2\bar{\sigma}^2 - \theta_1^2\right) \exp\left[\frac{(\theta_1 - \Delta\theta)^2}{2\bar{\sigma}^2} \right] + 4\Delta\theta \left(4\bar{\sigma}^2 + \theta_1^2\right) \exp\left[\frac{(\Delta\theta)^2}{2\bar{\sigma}^2} \right] \right. \\
&\quad \left. + (\theta_1 - 2\Delta\theta)\left(\theta_1^2 - 2\bar{\sigma}^2\right) \exp\left[\frac{(\theta_1 + \Delta\theta)^2}{2\bar{\sigma}^2} \right] \right\}.
\end{aligned} \tag{A3}$$

Following a similar procedure, we yield the following expression of $b_{\hat{\sigma}_{\mathrm{s}}^2}$:

$$\begin{aligned}
b_{\hat{\sigma}_{\mathrm{s}}^2} &= \frac{1}{2}\left(\frac{\partial^2 \hat{\sigma}_{\mathrm{s}}^2}{\partial \left(I_1\right)^2}\Big|_{\bar{I}_1} \sigma_{I_1}^2 + \frac{\partial^2 \hat{\sigma}_{\mathrm{s}}^2}{\partial \left(I_2\right)^2}\Big|_{\bar{I}_2} \sigma_{I_2}^2 + \frac{\partial^2 \hat{\sigma}_{\mathrm{s}}^2}{\partial \left(I_3\right)^2}\Big|_{\bar{I}_3} \sigma_{I_3}^2 \right) \\
&= \frac{1}{2}\left[\frac{-\theta_1^2 (C_1 + C_2 - 2)}{I_1^2 (C_1 + C_2)^3} + \frac{2\theta_1^2 (C_1 + C_2 + 4)}{I_2^2 (C_1 + C_2)^3} + \frac{-\theta_1^2 (C_1 + C_2 - 2)}{I_3^2 (C_1 + C_2)^3} \right] \\
&= \frac{1}{2}\left\{ \frac{2\bar{\sigma}^7 - \theta_1^2 \bar{\sigma}^5}{\sigma_\theta I_0 I_{\mathrm{R}} \theta_1^4} \exp\left[\frac{\left(\theta_1 - \Delta\bar{\theta}\right)^2}{2\bar{\sigma}^2} \right] + \frac{8\bar{\sigma}^7 + 2\theta_1^2 \bar{\sigma}^5}{\theta_1^4 \sigma_\theta I_0 I_{\mathrm{R}}} \exp\left[\frac{\left(\Delta\bar{\theta}\right)^2}{2\bar{\sigma}^2} \right] + \frac{2\bar{\sigma}^7 - \theta_1^2 \bar{\sigma}^5}{\theta_1^4 \sigma_\theta I_0 I_{\mathrm{R}}} \exp\left[\frac{\left(\theta_1 + \Delta\bar{\theta}\right)^2}{2\bar{\sigma}^2} \right] \right\} \\
&= \frac{\bar{\sigma}^5}{2\sigma_\theta I_0 I_{\mathrm{R}} \theta_1^4} \left\{ \left(2\bar{\sigma}^2 - \theta_1^2\right) \exp\left[\frac{\left(\theta_1 - \Delta\bar{\theta}\right)^2}{2\bar{\sigma}^2} \right] + \left(8\bar{\sigma}^2 + 2\theta_1^2\right) \exp\left[\frac{\left(\Delta\bar{\theta}\right)^2}{2\bar{\sigma}^2} \right] + \left(2\bar{\sigma}^2 - \theta_1^2\right) \exp\left[\frac{\left(\theta_1 + \Delta\bar{\theta}\right)^2}{2\bar{\sigma}^2} \right] \right\}.
\end{aligned} \tag{A4}$$

Equations (A3) and (A4) can be further simplified to the following forms

$$\begin{cases} b_{\Delta\hat{\theta}} = f(\theta_1) + 4f(0) + f(-\theta_1), \\ b_{\hat{\sigma}_s^2} = g(\theta_1) + 4g(0) + g(-\theta_1), \end{cases} \tag{A5}$$

where

$$\begin{cases} f(x) = \dfrac{(2\Delta\bar{\theta} + x)\, g(x)}{\bar{\sigma}^2}, \\ g(x) = \dfrac{\bar{\sigma}^5 \left(4\bar{\sigma}^2 - 3x^2 + \theta_1^2\right)}{8 I_0 \sigma_\theta \bar{I}_R \theta_1^4} \exp\left[\dfrac{(x - \Delta\bar{\theta})^2}{2\bar{\sigma}^2}\right]. \end{cases} \tag{A6}$$

References

[1] Endrizzi M 2018 *Nucl. Instrum. Method A* **878** 88

[2] Chapman D, Thomlinson W, Johnston R E, Washburn D, Pisano E, Guür N, Zhong Z, Menk R, Arfelli F and Sayers D 1997 *Phys. Med. Biol.* **42** 2015

[3] Pagot E, Cloetens P, Fiedler S, Bravin A, Coan P, Baruchel J, Hartwig J and Thomlinson W 2003 *Appl. Phys. Lett.* **82** 3421

[4] Rigon L, Besch H J, Arfelli F, Menk R H, Heitner G and Besch H P 2003 *J. Phys. D: Appl. Phys.* **36** A107

[5] Hu C H, Zhang L, Li H and Luo S Q 2008 *Opt. Express* **16** 16704

[6] Connor D M and Zhong Z 2014 *Curr. Radiol. Rep.* **2** 55

[7] Wei C X, Wu Z, Wali F, Wei W B, Bao Y, Luo R H, Wang L, Liu G and Tian Y C 2017 *Chin. Phys. B* **26** 108701

[8] Wang Z L, Liu D L, Zhang J, Huang W X, Yuan Q X, Gao K and Wu Z 2018 *J. Synchrotron Rad.* **25** 1206

[9] Wernick M N, Wirjadi O, D Chapman D, Z Zhong Z, N P Galatsanos N P, Yang Y, Brankov J G, Oltulu O, Anastasio M A and Muehleman C 2003 *Phys. Med. Biol.* **48** 3875

[10] Wang Y B, Li G P, Pan X D and Zheng S C 2015 *Nucl. Instrum. Method A* **770** 182

[11] Ji X, Ge Y S, Zhang R, Li K and Chen G H 2017 *Med. Phys.* **44** 2453

[12] Kiss M Z, Sayers D E and Zhong Z 2003 *Phys. Med. Biol.* **48** 325

[13] Chou C, Anastasio M A, Brankov J G, Wernick M N, Brey E M, Connor D M and Zhong Z 2007 *Phys. Med. Biol.* **52** 1923

[14] Yang H, Xuan R J, Hu C H and Duan J H 2014 *Chin. Phys. B* **23** 048701

[15] Faiz W, Zhu P, Hu R F, Gao K, Wu Z, Bao Y and Tian Y C 2017 *Chin. Phys. B* **26** 120601

[16] Zhang C, Pan X D, Shang H J and Li G 2018 *J. Appl. Phys.* **124** 164906

[17] Rigon L, Arfelli F and Menk R H 2007 *J. Phys. D: Appl. Phys.* **40** 3077

[18] Abrami A, Arfelli F, Barroso R C, *et al.* 2005 *Nucl. Instrum. Method A* **548** 221

[19] Zhao X J, Zhang K, Hong Y L, Huang W X, Yuan Q X, Zhu P P and Wu Z Y 2013 *Acta Phys. Sin.* **62** 124202 (in CHinese)

[20] Arfelli F, Astolfo A, Rigon L and Menk R H 2018 *Sci. Rep.* **8** 362

[21] Jia X, Ge Y S, Zhang R, Li K and Chen G H *Conference on Medical Imaging - Physics of Medical Imaging*, March 13–16, 2017, Orlando, USA, p. 1013219

[22] Bao Y, Wang Y, Li P Y, Wu Z, Shao Q G, Gao K, Wang Z L, Ju Z Q, Zhang K, Yuan Q X, Huang W X, Zhu P P and Wu Z Y 2015 *J. Synchrotron Rad.* **22** 786